coatings

MDPI

Article

Temperature-Controlled Molten-Salt Treatment of Co-Coated Ni Substrates to Form Porous Electrodes for Alkaline Hydrogen and Oxygen Evolution Reactions

Dawid Kutyła [1,*], Michihisa Fukumoto [2,*], Ryuu Takahashi [2], Katarzyna Skibińska [1], Piotr Palimąka [1] and Piotr Żabiński [1]

[1] Faculty of Non-Ferrous Metals, AGH University of Krakow, 30-059 Krakow, Poland; zabinski@agh.edu.pl (P.Ż.)
[2] Graduate School of Engineering Science, Akita University, Akita 010-8502, Japan
* Correspondence: kutyla@agh.edu.pl (D.K.); fukumoto@gipc.akita-u.ac.jp (M.F.)

Highlights

What are the main findings?

- Raising treatment temperature from 750 to 900 °C coarsened and thickened porous Ni–Co layers.
- Double-layer capacitance peaked at 825 °C, reaching 6.97 mF cm^{-2}.
- The 900 °C electrode reached a HER overpotential of 109 mV after 2 h at −10 mA cm^{-2}.
- Apparent OER Tafel slopes were lowest at 750 °C; final overpotentials were lowest at 900 °C. Laser energy density governs interfacial diffusion, phase distribution, and local misorientation.

What are the implications of the main findings?

- Higher double-layer capacitance does not necessarily indicate better HER/OER performance.
- Temperature control enables tuning of porous Ni–Co layers without changing the precursor.
- The 900 °C coating is promising as a bifunctional electrode for alkaline HER and OER.

Abstract

In this work, porous coatings were obtained by Co electrodeposition on Ni, followed by Al deposition and anodic dissolution in a NaCl–KCl–AlF_3 melt at 750, 825 and 900 °C. The same Co-coated Ni precursor, applied potentials and 3600 s Al-deposition time were used at all temperatures; the recorded anodic durations and transferred charges differed. SEM observations showed a change from a fine sponge-like surface to a coarser porous network. The estimated layer thicknesses were 8–12, 32–55 and 50–65 µm, respectively. The main XRD reflections were consistent with an fcc metallic phase in Co-rich material, with possible overlapping signals from Ni. Weak additional reflections were tentatively associated with Al-containing phases, but their identity was not confirmed. The highest apparent capacitance estimate was obtained at 825 °C. In 1 M NaOH, the lowest HER overpotentials among the treated electrodes were registered for the 900 °C sample: 109 and 494 mV after 2 h at −10 and −100 mA cm^{-2}. For OER, the lowest apparent Tafel slope was obtained at 750 °C, while the lowest end-of-test overpotentials were obtained at 900 °C. Unmodified Ni showed higher anodic currents in part of the polarisation range, so the treatment did not give a general improvement in OER compared with Ni. No post-measurement iR correction was applied. The measured electrodes showed different trends in morphology,

Check for updates

Academic Editors: Marin Kurtela and Marina Samardzija

Received: 21 September 2026
Revised: 31 October 2026
Accepted: 2 November 2026
Published: 4 November 2026

Copyright: © 2026 by the authors. Licensee MDPI, Basel, Switzerland. This article is an open access article distributed under the terms and conditions of the Creative Commons Attribution (CC BY) license.

apparent capacitance and HER/OER response; statistical significance and between-electrode reproducibility were not established.

Keywords: co-coated Ni substrates; molten-salt treatment; aluminium electrodeposition; selective dissolution; porous coatings; hydrogen evolution reaction; oxygen evolution reaction

1. Introduction

Alkaline water electrolysis is an established method of hydrogen production. Further improvement of this technology requires active, durable and inexpensive electrodes which can be prepared using scalable coating techniques [1–5]. Nickel is widely used in alkaline electrolysers due to its electrical conductivity and corrosion resistance [5,6]. However, compact Ni requires relatively high overpotentials for hydrogen and oxygen evolution. The performance of the electrodes is connected with reaction kinetics, the number of accessible surface sites, wetting and gas-bubble release [6–10].

In alkaline HER, hydrogen is formed from water molecules rather than directly from protons. This reaction includes water dissociation, hydrogen adsorption and subsequent electrochemical or chemical desorption [7–10]. For porous electrodes, the response also depends on electrolyte access, removal of OH− and detachment of H_2 bubbles [8–12]. During OER, the surface chemistry of Ni-based electrodes is strongly affected by the formation of hydroxides and oxyhydroxides [13–16]. Therefore, a morphology favourable for HER does not necessarily give the same temperature trend in OER.

Co is often added to Ni-based electrodes used in alkaline electrocatalysis. For electrodeposited Ni–Co materials, the HER response depends on composition, deposition conditions and porous morphology [17–22]. When comparing HER and OER, it is therefore necessary to consider both the coating morphology and the surface state during polarisation.

Another main approach to improving Ni-based electrocatalysts is surface development. Raney-type Ni is a classical example, usually obtained by selective leaching of Al or Zn from Ni-based precursor alloys [23–31]. Its high apparent activity is commonly connected with a large real surface area, a defect-rich metallic skeleton and a porous network that allows electrolyte penetration into the electrode. However, the activity is not determined by surface area alone. The phase composition of the precursor, the dissolution process, ligament coarsening, residual alloying elements and mechanical integrity of the porous layer also affect the catalytic response [23–31]. During dealloying, the less noble component is selectively dissolved, while surface diffusion or rearrangement of the remaining atoms produces a porous metallic network [32–34]. The pore size, ligament thickness and connectivity therefore depend on the precursor phases, dissolution conditions and temperature-dependent diffusion processes. Al-containing precursors are particularly useful for Ni-based porous electrodes because Al can be used as a sacrificial element and Al–Ni intermetallic phases readily form at elevated temperatures. The Al–Ni system contains several stable phases, including NiAl, Ni3Al and Al-rich nickel aluminides. Reaction-diffusion studies have shown that their growth is strongly affected by temperature, diffusion kinetics and Kirkendall-type effects [35–38]. Stable aluminides are also present in the Co–Al system, including CoAl and Al-rich cobalt aluminides. A Co-rich surface exposed to liquid Al may therefore follow a different reaction pathway from a Ni-rich surface [39,40]. The Co–Ni system shows mainly metallic solid-solution behaviour over a broad composition range, with fcc/hcp stability depending on composition and temperature [41]. The phase equilibria of the Al–Co–Ni system provide a thermodynamic basis for considering possible Al-containing reaction products [42]. For a Co-coated Ni precursor, the reaction sequence may also depend on contact of the outer Co layer with the deposited Al and the underly-

ing Ni substrate. Molten-salt Al deposition followed by anodic dissolution allows porous metallic coatings to be obtained without preparing a bulk Al-containing alloy before the experiment. Al is deposited from a chloride–fluoride melt on the metallic substrate at high temperature. Above its melting point, the deposited Al is liquid and can react rapidly with the exposed metal, forming Al-containing intermetallic regions. Subsequent anodic polarisation selectively removes Al from the modified region and leaves a porous metallic framework on the substrate [43–49]. Compared with conventional powder metallurgy or chemical-leaching methods, Al deposition, intermetallic formation and selective dissolution can be carried out in the same high-temperature electrochemical environment. Coating preparation, intermetallic transformation and dealloying are therefore combined in one surface-engineering process.

Previous studies have shown that Al deposition and dissolution in molten salts can be used to obtain porous Ni, Ni–Co, Ni–Pt, stainless-steel-based and noble-metal-modified Ni electrodes [44–49]. For porous Ni, this treatment substantially increased the electrochemically accessible surface and improved the activity in alkaline oxidation reactions [46]. The results obtained for stainless steel showed that the method is not limited to pure Ni substrates and can also produce porous functional surfaces from multicomponent alloys [48]. For Ni–Pt electrodes, the distribution of Pt inside the porous structure was important. Electrodes with exposed Pt-rich porous layers showed substantially better HER response than structures where Pt was less accessible inside the porous body [47]. Work on multicomponent coatings also showed that selective dissolution, surface oxidation and element redistribution can strongly affect catalytic behaviour, particularly when Al-containing regions modify the surface reactivity [50]. Ni–Co electrodes are of interest because they contain no noble metals and are strongly affected by phase-transformation pathways. Recent work on layered Ni–Co and Ni–Co–Ni electrodes showed that the initial arrangement of the layers controls the main Al-driven reaction route [49]. When Co was directly exposed to liquid Al, the process was mainly connected with Co–Al-derived intermetallic formation and produced a highly open Co-containing porous network. When the Co-rich layer was covered by an outer Ni layer, the reaction shifted towards Ni–Al formation. A more compact Ni-rich surface was obtained, with different HER kinetics [49]. These results showed that the response of molten-salt-derived porous electrodes is not determined only by their nominal elemental composition. The initial layer arrangement can determine the sequence of intermetallic formation, selective dissolution, element redistribution and the final electrochemical behaviour.

Earlier molten-salt studies compared substrate composition, noble-metal modification and different precursor layer sequences [44–49]. The Ni–Co/Ni–Co–Ni comparison showed the importance of layer arrangement [49]. Treatment temperature can also affect reaction-layer growth and pore evolution [32–38]. Its influence on the same Co-coated Ni precursor therefore needs a separate comparison.

In this work, Co-coated Ni substrates were treated at 750, 825 and 900 °C using the same applied potentials and Al-deposition time. The anodic stage was ended when the current approached zero, so its duration and the transferred charges differed between temperatures. In the earlier study, different layer sequences were compared [49]. Here, the starting structure was kept the same: an electrodeposited Co layer on a compact Ni plate. SEM/EDS, XRD, capacitance measurements, polarisation curves and 2 h chronopotentiometry were used to compare the final porous coatings. The comparison describes the electrodes obtained under these treatment conditions, rather than temperature at matched charge and anodic duration. The final material is described as a porous coating formed on Ni; this does not imply a homogeneous Ni–Co alloy with a predetermined composition.

2. Materials and Methods

2.1. Materials and Substrate Preparation

Compact nickel plates with a purity of 99.9% were used as substrates. The dimensions of the samples were approximately 15 mm × 10 mm × 1 mm. The geometric surface area exposed to the electrolyte during electrochemical measurements was approximately 1.6 cm^2. Before electrodeposition, the samples were polished with SiC abrasive paper up to #800 grit. They were then ultrasonically cleaned in acetone and ethanol, rinsed with deionised water and dried in air.

2.2. Cobalt Electrodeposition

Co was electrodeposited directly on the Ni substrate (Nilaco Corporation, Tokyo, Japan) from an aqueous bath containing 500 g L^{-1} $CoSO_4 \cdot 7H_2O$, 15 g L^{-1} NaCl and 45 g L^{-1} H_3BO_3 (Nacalai Tesque, Inc., Kyoto, Japan). The bath pH was approximately 3.5, and the temperature was 50 °C. Deposition was carried out galvanostatically at 30 mA cm^{-2} for 60 min (3600 s) with a Pt anode. The continuous Co-rich layer had a thickness of approximately 30 µm, estimated from cross-sectional observations. After deposition, the samples were rinsed with deionised water and dried in air.

2.3. Molten-Salt Al Deposition and Selective Dissolution

The Co-coated Ni samples were fixed in a molybdenum holder and immersed in the molten salt electrolyte. The bath consisted of 48.25 mol% NaCl, 48.25 mol% KCl and 3.5 mol% AlF_3. Treatment was carried out at 750, 825 and 900 °C under flowing Ar. A graphite electrode was used as the counter electrode. The Ag/AgCl reference electrode consisted of an Ag wire immersed in a NaCl–KCl–AgCl melt in a mullite housing.

Al deposition was carried out potentiostatically at −1.4 V vs. Ag/AgCl for 3600 s. At these temperatures, the deposited Al is liquid and can react with the Co-rich surface layer and, depending on temperature, with the underlying Ni-containing region. After deposition, the potential was changed to −0.7 V to dissolve metallic Al and Al-rich intermetallic regions. The anodic stage was ended when the current approached zero. This was a practical endpoint and did not establish complete Al removal. The recorded anodic stages lasted approximately 2534, 3241 and 2393 s at 750, 825 and 900 °C, respectively. After treatment, the samples were removed from the melt, cooled and washed with deionised water to remove residual salt. Equal charges, amounts of Al and current efficiencies were not assumed for the deposition and dissolution processes. The charge per unit area was calculated by trapezoidal integration as $q = 3.6 \int |j| dt$, with j in mA cm^{-2} and t in h. The cathodic interval was 0–1 h, and the anodic interval extended from 1 h to the final recorded point. Values at the 1 h boundary were interpolated linearly and segments crossing zero were split at the crossing. The cathodic charge values were 272.96, 384.35 and 491.11 C cm^{-2}, and the anodic charge values were 235.76, 263.40 and 364.55 C cm^{-2}, respectively. The anodic-to-cathodic ratios were 86.37%, 68.53% and 74.23%.

2.4. Structural and Phase Characterization

The surface morphology and cross-sections of the samples were examined using a scanning electron microscope (JEOL 6000, Tokyo, Japan). For cross-sectional observations, the samples were embedded in conductive resin, ground and polished. The distributions of Ni, Co, Al and O were analysed by energy-dispersive X-ray spectroscopy coupled with SEM. The porous-layer thickness was estimated from the cross-sectional images. XRD measurements were performed using Cu Kα radiation (Rigaku Miniflex, Japan). The registered patterns were compared with JCPDS/ICDD reference cards. The main reflections were described as a metallic fcc phase consistent with Co-rich material, with possible

overlapping signals from Ni. The weak additional reflections were treated as tentative Co–Al-related phases.

2.5. Electrochemical Measurements

Electrochemical measurements were carried out at room temperature in 1 M NaOH. A three-electrode cell was used, with the tested sample as the working electrode, Pt mesh as the counter electrode and Hg/HgO as the reference electrode. Measurements were performed using a Biologic SP-300 potentiostat (France) with EC-Lab software, version 11.62. Before polarisation, the electrodes were allowed to stabilise at open-circuit potential. For each treatment temperature, one selected electrode was tested. Repeated CV scans were recorded on the same electrode, so variability between independently prepared electrodes could not be determined. Three CV scans were recorded at each scan rate on the same electrode. These scans are not independent electrode replicates. Differences in capacitance, apparent Tafel slopes and overpotentials describe the measured electrodes only; their statistical significance and between-electrode reproducibility were not established.

All potential values were recalculated to the reversible hydrogen electrode according to: $E_{RHE} = E_{Hg/HgO} + 0.098\ V + 0.0591 \times pH$, where 0.098 V is the standard potential of the Hg/HgO reference electrode versus SHE at 25 °C. The pH of 1 M NaOH was taken as 14.0. The HER overpotential was calculated as $\eta_{HER} = |E_{RHE}|$ for cathodic potentials below 0 V vs. RHE. For OER, the overpotential was calculated as $\eta_{OER} = E_{RHE} - 1.23\ V$.

Linear sweep voltammetry for HER and OER was recorded at 20 mV s^{-1}. The current was normalised to the exposed geometric surface area. Apparent Tafel slopes were determined graphically from selected approximately linear parts of the $\log_{10}(|j|)$–E curves. Each line was extended to $|j| = 1$ and 10 mA cm^{-2}, and the absolute potential difference was taken as the slope over one decade, reported in mV dec^{-1}. These reference current densities do not define the measured fitting range. R^2 values were not obtained by this graphical method. No post-measurement iR correction was applied. The scan rate and uncompensated resistance can affect the registered slopes and overpotentials. Other current contributions cannot be excluded, so the slopes are treated as apparent values and are not used to identify a reaction mechanism or determine intrinsic activity.

Chronopotentiometric measurements were performed for 2 h at −10 and −100 mA cm^{-2} for HER and at 10 and 100 mA cm^{-2} for OER. Unmodified Ni was also tested as a comparison electrode. Apparent capacitance was estimated from CV recorded in a 100 mV-wide potential window. Three CV scans were recorded at each scan rate on the same electrode. The anodic and cathodic current densities were extracted separately and plotted against scan rate in Microsoft Excel. A straight line with a free intercept was fitted to each branch by ordinary least squares using scan rates of 0.010, 0.020, 0.050, 0.075, 0.100 and 0.150 V s^{-1}. The apparent areal capacitance was calculated as $C_{app} = (|s_a| + |s_c|)/2$, where s_a and s_c are the slopes of the anodic and cathodic current-density dependences on scan rate, respectively. For current density in mA cm^{-2} and scan rate in V s^{-1}, C_{app} is obtained in mF cm^{-2}. These values were not converted to absolute ECSA. Fitting $(j_a - j_c)/2$ directly against scan rate gives the same apparent capacitance when both branches use the same scan rates and equal weights.

3. Results and Discussion

3.1. Preparation of Porous Coatings on Co-Coated Ni Substrates

The main stages of porous coating preparation are presented in Figure 1. First, Co was electrodeposited on Ni from an aqueous solution. The obtained sample was then treated by Al deposition and anodic dissolution in molten salts. Al initially contacts the exposed Co-rich layer. The coating obtained at 750 °C was fine and relatively thin. At 825 °C, a thicker

porous network was observed, while treatment at 900 °C gave a coarser structure with larger openings. The cathodic charge exceeded the anodic charge at each temperature. This is consistent with incomplete Al removal, and the selected anodic potential may have been insufficient to dissolve all Co–Al regions. However, current efficiencies were not measured, so the charge difference cannot be converted directly as proof of Al presence or to identify a Co-Al specific phase.

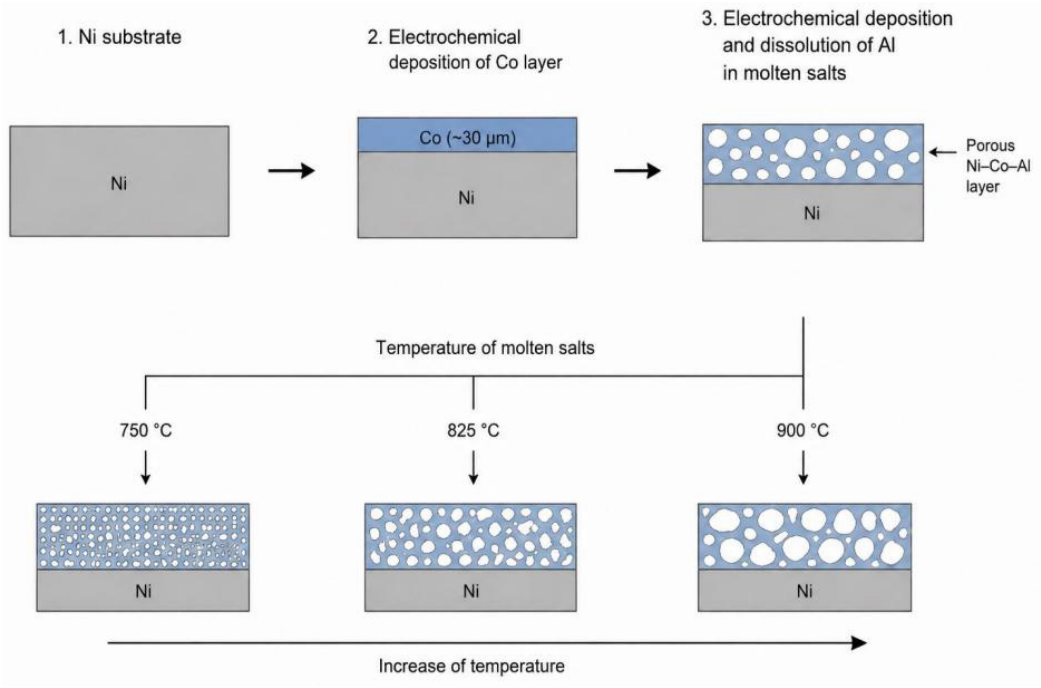


Figure 1. Graphical description of process. Co electrodeposition on a compact Ni substrate, followed by molten-salt Al deposition and anodic dissolution to form a porous surface layer.

3.2. XRD Analysis: fcc Metallic Reflections and Weak Additional Diffraction Features

The XRD patterns of the obtained porous electrodes formed on Ni are presented in Figure 2. The samples were treated at 750, 825 and 900 °C. The main reflections at approximately 44.18°, 51.65° and 75.90° are consistent with the (111), (200) and (220) reflections of an fcc metallic phase in Co-rich material. Signals from Ni may overlap with these reflections. Therefore, the patterns do not allow the separate Ni and Co contributions to be distinguished and do not confirm a homogeneous alloy. At 750 °C, the pattern was dominated by the fcc metallic reflections.

For the electrodes treated at 825 and 900 °C, weak additional signals were observed in the approximate 45.53–49.98° range and near 54.71°. These signals were tentatively assigned to Co_2Al_5 (Al_5Co_2) using reference card 00-048-1301 for comparison. Individual reference positions and Miller indices were not established, so this phase is only a claim. Screening of ICDD entries for Co-, Al- and Ni-containing phases gave fcc Co and Co_2Al_5 as the candidate matches, but did not resolve the additional feature on the lower-angle side of the main reflection in the 900 °C pattern. Al detected by EDS and the cathodic/anodic charge difference do not directly confirm the presence of this or any other specific phase.

The coatings obtained at higher temperatures showed weak additional signals in the XRD patterns and local Al signals in the EDS maps.

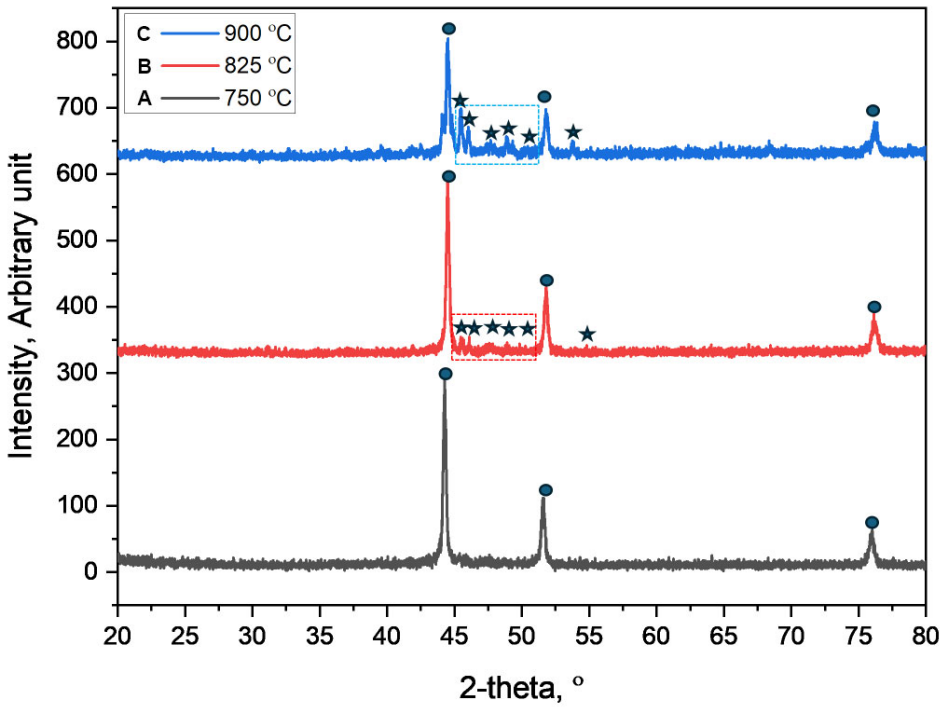


Figure 2. X-ray diffraction patterns of porous electrodes formed on Ni treated at (A) 750 °C (black), (B) 825 °C (red) and (C) 900 °C (blue). Circles indicate fcc metallic reflections consistent with Co-rich material, with possible overlapping Ni contributions. Stars indicate weak signals tentatively associated with Co_2Al_5. The peaks positions and interpretation is added in Table 1.

Table 1. Tentative XRD peak assignment for porous electrodes formed on Ni after molten-salt treatment.

2θ/°	Tentative Assignment	Reflection	JCPDS/ICDD Card	Interpretation
44.18	fcc metallic phase: Co-rich material, with possible overlapping contributions from Ni substrate	(111)	00-15-0806	dominant metallic phase
51.65	fcc metallic phase: Co-rich material, with possible overlapping contributions from Ni substrate	(200)	00-15-0806	dominant metallic phase
75.90	fcc metallic phase: Co-rich material, with possible overlapping contributions from Ni substrate	(220)	00-15-0806	dominant metallic phase
45.53–49.98	Weak signal: possible Co_2Al_5, tentative	hkl not established	00-048-1301	phase not confirmed
ca. 54.71	Weak signal: possible Co_2Al_5, tentative	hkl not established	00-048-1301	phase not confirmed

3.3. Top-View SEM: Pore Coarsening with Increasing Temperature

The top-view SEM images of the obtained electrodes are presented in Figure 3. A gradual change in surface morphology was observed with increasing treatment temperature. The sample treated at 750 °C had a fine, sponge-like surface with many small pore openings and narrow ligaments. Most openings were in the submicrometre to low-micrometre range. At 825 °C, larger and more open pores were observed, while the surface still contained

interconnected features. Treatment at 900 °C gave a coarse open-cell structure with larger pores, thicker ligaments and fewer small openings. The approximate pore-opening ranges were estimated manually from comparable 4000× SEM images using the scale bars in Figure 3. The values presented in Table 2 are semi-quantitative estimates.

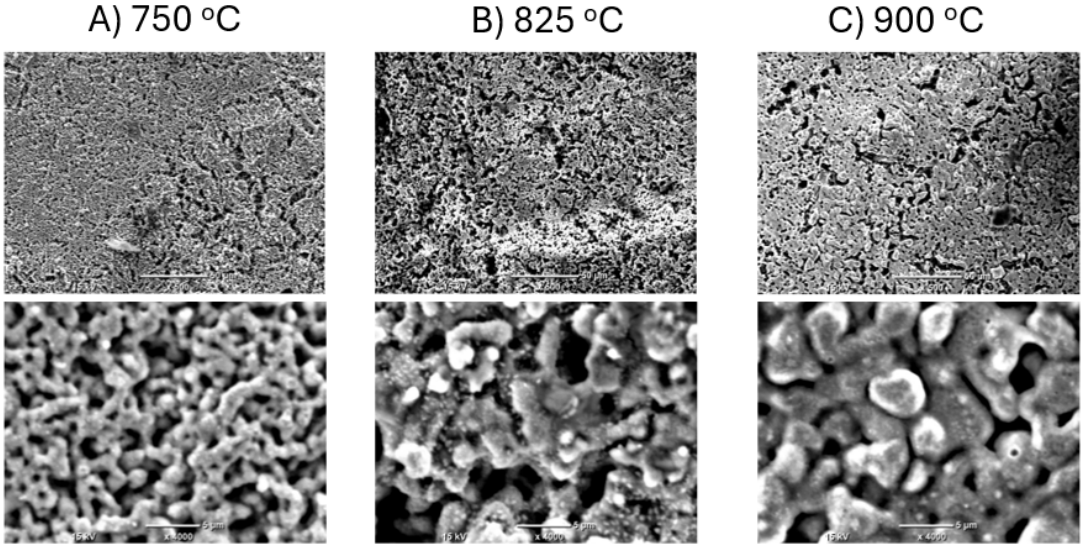


Figure 3. Top-view SEM images of porous electrodes formed on Ni obtained by molten-salt treatment at different temperatures: (**A**) 750 °C, (**B**) 825 °C and (**C**) 900 °C. Upper row: 500×; lower row: 4000×.

Table 2. Semi-quantitative surface morphology parameters from top-view SEM images.

Treatment Temperature	Dominant Pore Openings	Local Larger Voids	Morphological Interpretation
750 °C	ca. 0.3–1.2 µm	up to ca. 2 µm	fine sponge-like layer with numerous small pore openings
825 °C	ca. 0.7–2.5 µm	ca. 3–5 µm	intermediate, highly developed porous network
900 °C	ca. 1.5–4 µm	ca. 5–8 µm	coarse open-cell morphology

Table 2 summarises the fine morphology obtained at 750 °C, the intermediate porous network at 825 °C and the coarse structure at 900 °C.

3.4. Cross-Sectional SEM/EDS: Porous-Layer Growth and Elemental Redistribution

The cross-sectional SEM images in Figure 4 show that the obtained porous layer became thicker with increasing treatment temperature. The layer thickness was approximately 8–12 µm at 750 °C, 32–55 µm at 825 °C and 50–65 µm at 900 °C. These ranges were estimated from the images and should be treated as approximate values.

The EDS maps presented in Figures 5–7 show a Co-rich outer region and a Ni-rich substrate. Local signals from Al and O were also registered. In Figure 5, the dark area on the left side, outside the apparent sample boundary, is the mounting resin. The local Al signal in this area is attributed to Al-containing material mechanically transferred from the coating onto the adjacent resin during polishing. This feature was observed only at this location in the sample treated at 750 °C. The affected resin region is treated as a local sample-preparation artefact and is not used as evidence for Al retained in the coating. The Al map is interpreted qualitatively within the sample boundary. The cathodic/anodic charge imbalance is consistent with incomplete Al removal, but does not identify the source of the outside EDS signal. EDS gives information about elemental distribution but does not

identify aluminide, oxide or hydroxide phases. The general description of the EDS images is concluded in Table 3.

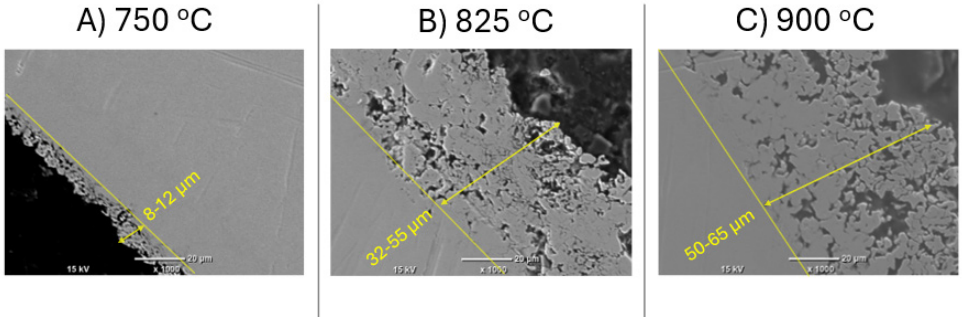


Figure 4. Cross–sectional SEM images of porous electrodes formed on Ni obtained by molten-salt treatment at different temperatures: (**A**) 750 °C, (**B**) 825 °C and (**C**) 900 °C. The yellow lines indicate the estimated thickness of the porous layer.

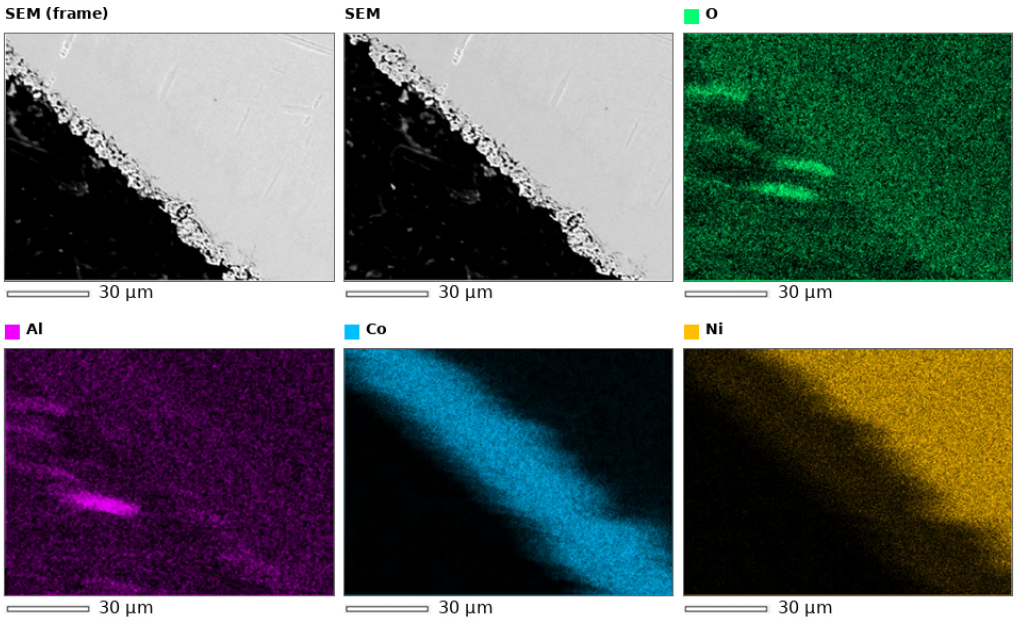


Figure 5. Cross-sectional SEM images and corresponding EDS elemental maps of the porous coating formed on Ni treated at 750 °C. Element colours are consistent throughout Figures 5–7: O (green), Al (magenta), Co (cyan) and Ni (gold). Scale bars: 30 µm. The dark area on the left side outside the sample is a conductive resin. The local Al signal in this region is attributed to mechanical transfer of Al-containing material during polishing and is excluded from interpretation of the coating composition.

Table 3. Structural characteristics of porous coatings formed on Ni treated at different temperatures.

Temperature	Porous-Layer Thickness	Main XRD Response	Residual Al-Containing Regions	Main Morphological Feature
750 °C	ca. 8–12 µm	fcc metallic reflections	weak or not clearly detected by XRD	fine sponge-like surface
825 °C	ca. 32–55 µm	fcc metallic reflections + weak additional diffraction features	locally visible by EDS	developed porous network
900 °C	ca. 50–65 µm	fcc metallic reflections + weak additional diffraction features	locally visible by EDS	coarse open-cell structure

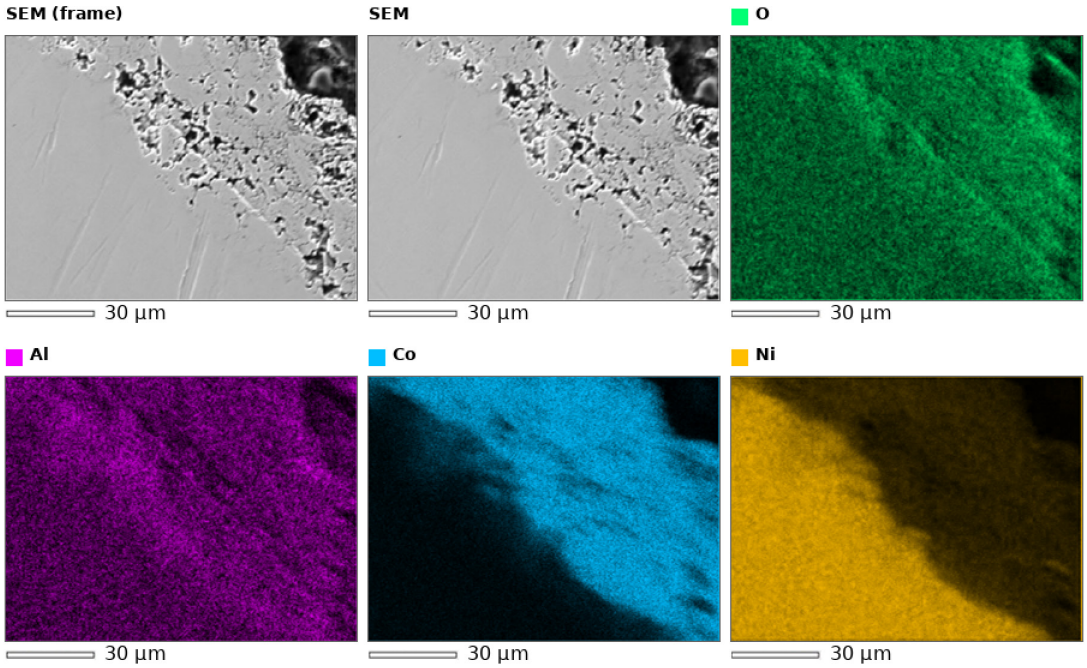


Figure 6. Cross-sectional SEM images and corresponding EDS elemental maps of the porous coating formed on Ni treated at 825 °C. Element colours follow the key in Figure 5. Scale bars: 30 µm.

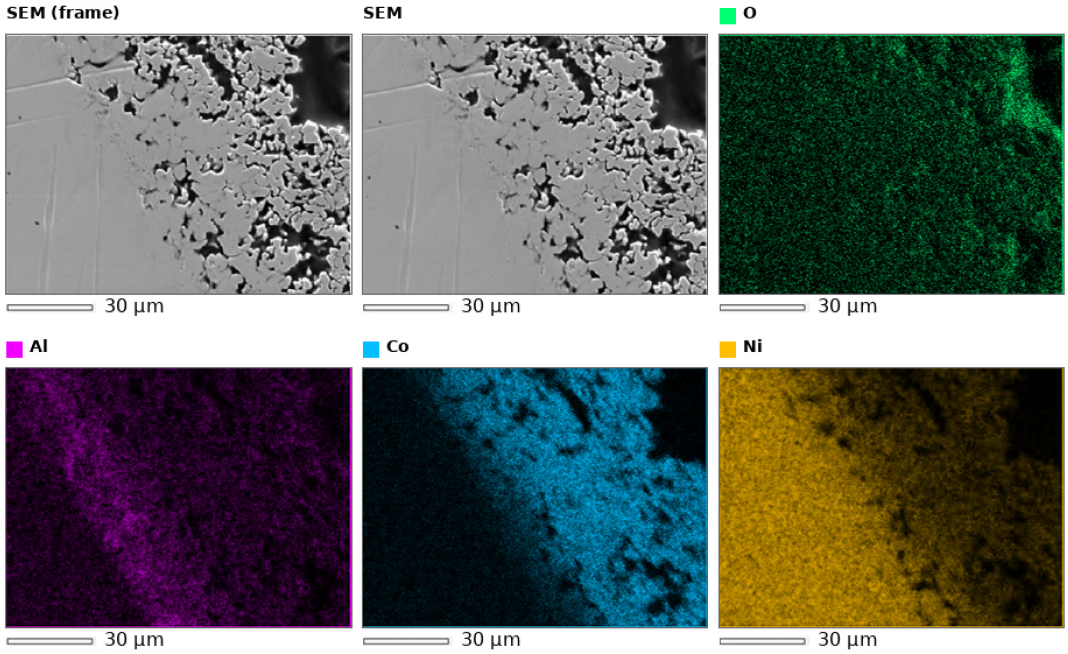


Figure 7. Cross-sectional SEM images and corresponding EDS elemental maps of the porous coating formed on Ni treated at 900 °C. Element colours follow the key in Figure 5. Scale bars: 30 µm.

The thicker layers obtained at higher temperatures may be connected with changes in Al mobility and interdiffusion during treatment. However, the SEM/EDS measurements show the samples after treatment. They do not allow the separate contributions of these processes or the extent of Al removal to be determined.

3.5. Apparent Capacitance Estimates from CV

The apparent capacitance estimates obtained from the CV measurements in Figure 8 were 5.87, 6.98 and 5.78 mF cm^{-2} for the electrodes treated at 750, 825 and 900 °C, respectively.

The highest value was obtained at 825 °C, although the thickest coating was observed at 900 °C. Capacitance also depends on the specific properties of the exposed surface. Therefore, the differences between these values cannot be explained only by the accessible surface area.

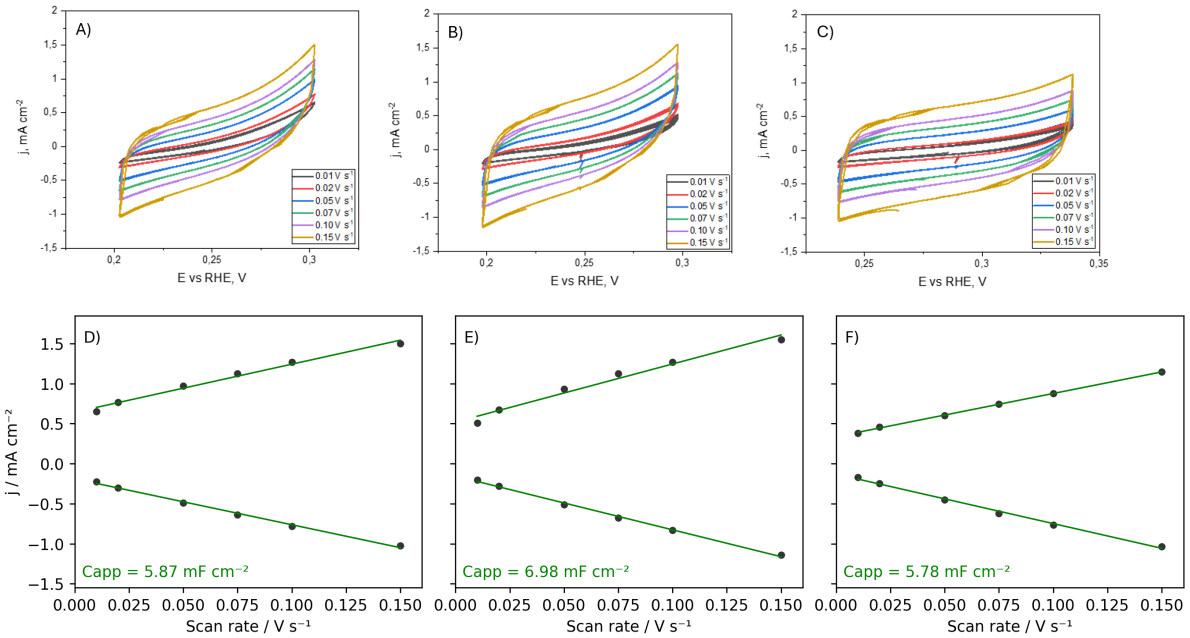


Figure 8. CV measured at different scan rates for porous electrodes formed on Ni treated at (**A**) 750 °C, (**B**) 825 °C and (**C**) 900 °C. Graphs (**D**–**F**) show the scan-rate dependence of the anodic and cathodic current densities used to estimate apparent capacitance. Horizontal axes in (**D**–**F**): scan rate, V s^{-1}. Panels (**D**–**F**) use the corrected six-point fits and apparent capacitances of 5.87, 6.98 and 5.78 mF cm^{-2}, respectively. Green lines and labels mark the corrected fits and values. The intermediate scan rate used in these fits was 0.075 V s^{-1}; it is displayed as 0.07 V s^{-1} in the original CV-graphs legend.

3.6. Hydrogen Evolution Reaction

The HER polarisation curves and apparent Tafel plots are presented in Figure 9. The registered cathodic current magnitudes were higher for the treated electrodes than for unmodified Ni over the displayed range. The difference was most visible for the samples treated at 825 and 900 °C. The apparent slope magnitude was approximately 300 mV dec^{-1} for Ni and decreased to 241, 138 and 116 mV dec^{-1} for the electrodes treated at 750, 825 and 900 °C, respectively. Thus, a decrease was observed for every treatment temperature, with the largest differences at 825 and 900 °C. These graphical apparent slopes describe the individual measured electrodes and are not statistically substantiated differences between treatment temperatures.

The registered potential during the 2 h HER chronopotentiometric measurements is presented in Figure 10. At −10 mA cm^{-2}, the end-of-test overpotentials were 152, 131 and 109 mV for the samples treated at 750, 825 and 900 °C, respectively. At −100 mA cm^{-2}, the corresponding values were 559, 518 and 494 mV. The electrode treated at 900 °C gave the lowest HER overpotential in this temperature series, although its apparent capacitance estimate was lower than that of the sample treated at 825 °C. This response may be related to easier electrolyte access and gas removal, but neither process was measured directly. The overpotential differences are descriptive; between-electrode variability was not determined.

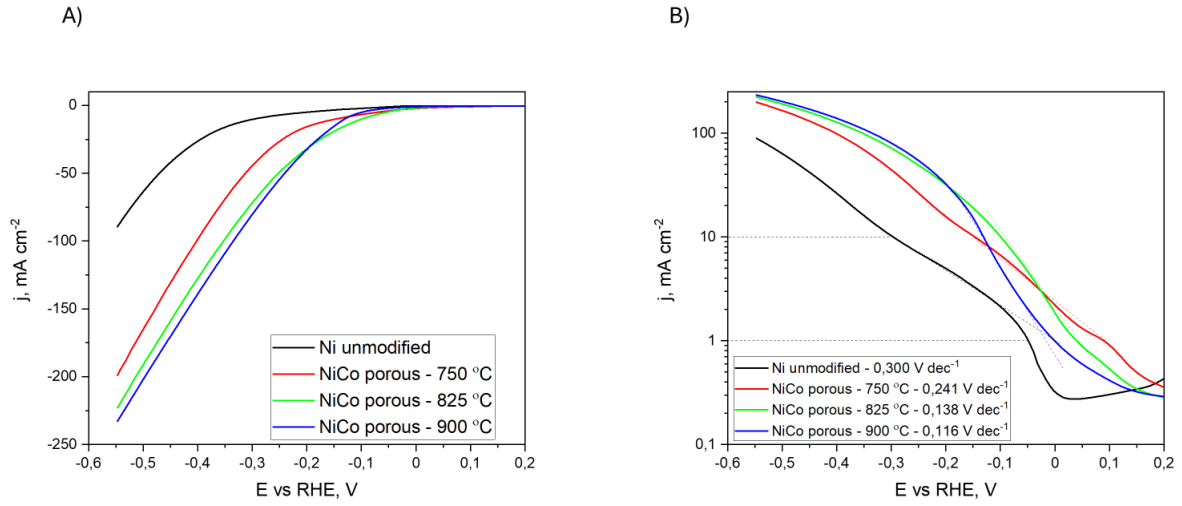


Figure 9. (**A**) HER polarisation curves and (**B**) apparent Tafel plots for unmodified Ni and porous electrodes formed on Ni treated at 750, 825 and 900 °C. Electrolyte: 1 M NaOH; scan rate: 20 mV s^{-1}. Current densities are normalised to geometric area; no post-measurement iR correction was applied. Slopes are reported as positive magnitudes. The 1–10 mA cm^{-2} interval is a reference interval on extrapolated lines, not necessarily the measured fitting range.

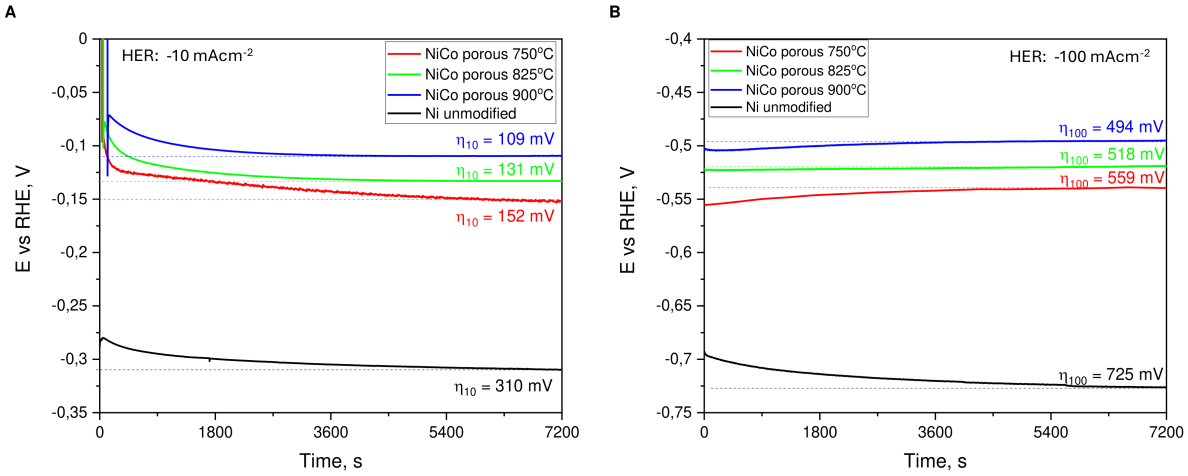


Figure 10. Short-term chronopotentiometric HER response of unmodified Ni (black) and porous electrodes formed on Ni treated at 750 °C (red), 825 °C (green) and 900 °C (blue), at (**A**) −10 and (**B**) −100 mA cm^{-2} in 1 M NaOH. Measurements cover 7200 s (2 h).

3.7. Oxygen Evolution Reaction

The OER polarisation curves and apparent Tafel plots are presented in Figure 11. In part of the higher-potential range, the registered anodic current densities were higher for unmodified Ni than for the treated electrodes. These curves therefore do not confirm a general improvement in OER performance over Ni. The apparent slope magnitudes were 123, 134 and 157 mV dec^{-1} for the electrodes treated at 750, 825 and 900 °C, respectively, compared with approximately 163 mV dec^{-1} for Ni. The lowest slope obtained at 750 °C alone does not mean that this electrode had the highest OER activity. Changes in Ni/Co hydroxide or oxyhydroxide surface chemistry may contribute to the anodic response, but the active species were not characterised. These apparent slope differences were not tested for statistical significance.

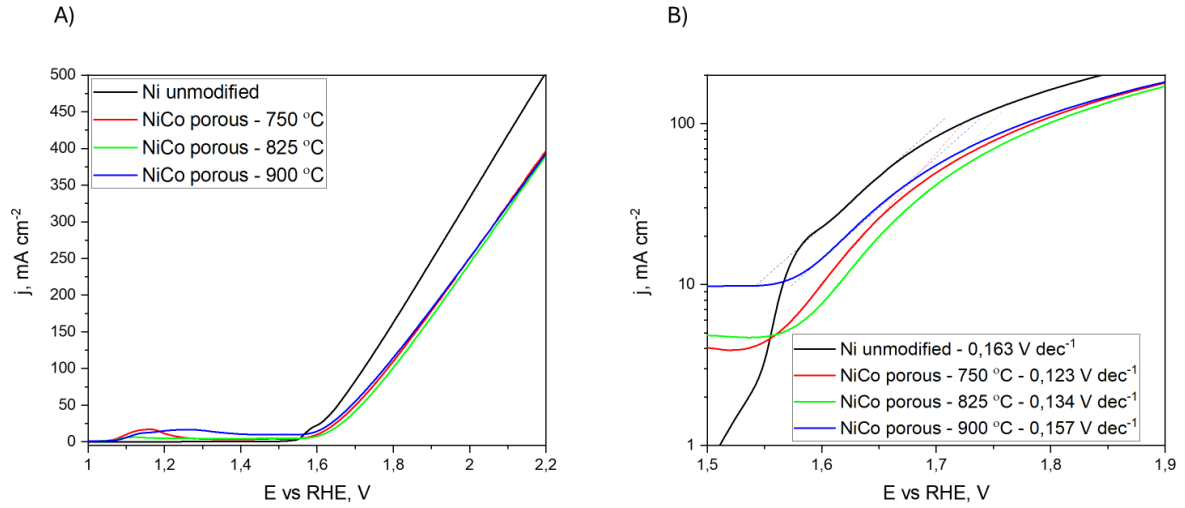


Figure 11. (**A**) OER polarisation curves and (**B**) apparent Tafel plots for unmodified Ni and porous electrodes formed on Ni treated at 750, 825 and 900 °C. Electrolyte: 1 M NaOH; scan rate: 20 mV s^{-1}. Current densities are normalised to geometric area; no post-measurement iR correction was applied. The 1–10 mA cm^{-2} interval is used to read potentials from extrapolated lines and is not necessarily the measured range used to select the lines.

The registered potential during the 2 h OER chronopotentiometric measurements is presented in Figure 12. At 10 mA cm^{-2}, the end-of-test overpotentials were 509, 502 and 493 mV for the samples treated at 750, 825 and 900 °C, respectively. At 100 mA cm^{-2}, the corresponding values were 881, 881 and 870 mV. The lowest end-of-test overpotential among the treated electrodes was obtained at 900 °C, while the lowest apparent OER Tafel slope was obtained at 750 °C. These two measurements therefore show different temperature trends. Resistance, wetting, changes in the surface state and gas evolution may contribute to this difference, but their separate effects were not measured. The obtained results are summarised in Table 4A,B. The differences between the end-of-test overpotentials describe the measured electrodes only; between-electrode variability was not determined.

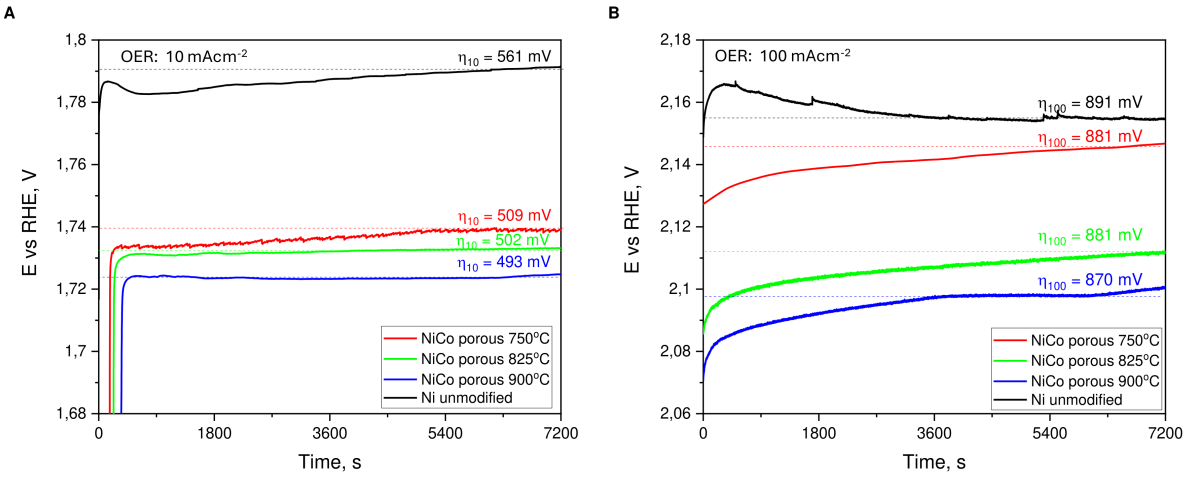


Figure 12. Short-term chronopotentiometric OER response of unmodified Ni (black) and porous electrodes formed on Ni treated at 750 °C (red), 825 °C (green) and 900 °C (blue), at (**A**) 10 and (**B**) 100 mA cm^{-2} in 1 M NaOH. Measurements cover 7200 s (2 h).

Table 4. (**A**). Structural characteristics and provisional capacitance estimates of porous electrodes formed on Ni. (**B**). Electrochemical response of porous electrodes formed on Ni.

(**A**)			
Electrode	**Layer Thickness**	**Provisional Capacitance Estimate/mF cm^{-2}**	**Main Morphology**
Porous coating on Ni 750 °C	ca. 8–12 µm	5.87	fine sponge-like porous layer
Porous coating on Ni 825 °C	ca. 32–55 µm	6.98	developed porous network with limited coarsening
Porous coating on Ni 900 °C	ca. 50–65 µm	5.78	coarse open-cell morphology

(**B**)						
Electrode	**Apparent HER Tafel Slope Magnitude/ mV dec^{-1}**	**ηHER After 2 h at −10 mA cm^{-2}/mV**	**ηHER After 2 h at −100 mA cm^{-2}/mV**	**Apparent OER Tafel Slope Magnitude/ mV dec^{-1}**	**ηOER After 2 h at 10 mA cm^{-2}/mV**	**ηOER After 2 h at 100 mA cm^{-2}/mV**
Porous coating on Ni 750 °C	241	152	559	123	509	881
Porous coating on Ni 825 °C	138	131	518	134	502	881
Porous coating on Ni 900 °C	116	109	494	157	493	870

Note: Electrochemical values are reported as apparent values because no post-measurement iR correction was applied. The values describe one electrode per treatment temperature; statistical significance and between-electrode reproducibility were not established.

The obtained results show that one treatment temperature does not give the best value for every measured quantity. The highest apparent capacitance estimate was obtained at 825 °C, the lowest end-of-test HER and OER overpotentials at 900 °C, and the lowest apparent OER Tafel slope at 750 °C. These differences show that layer thickness and capacitance alone do not explain the electrochemical response. Surface composition, resistance and the state of the surface during polarisation may also contribute.

The Pt-containing electrodes obtained by molten-salt treatment and presented in Table 5 showed lower HER overpotentials and Tafel slopes than the present porous electrodes formed on Ni. The measurements were performed using different protocols, so this comparison gives context rather than a direct activity ranking. In our work, treatment temperature was changed while the same non-noble precursor was used. In the earlier Ni–Co/Ni–Co–Ni study, changing the layer order changed the Co–Al versus Ni–Al reaction pathway. Here, the Co-coated Ni precursor was kept the same, while the recorded anodic durations and transferred charges differed. The coatings obtained at different temperatures were compared using layer thickness, morphology, diffraction features, apparent capacitance and HER/OER response.

Table 5. Comparison of molten-salt-derived porous systems and their main controlling variables.

System	**Main Controlled Variable**	**Electrolyte**	**Representative Result**	**Main Conclusion**
Porous Ni	Al deposition/dissolution on Ni	alkaline medium	Cdl increased from 0.29 to 2.16 mF cm^{-2} in previous UOR-oriented tests	molten-salt treatment strongly increases Ni surface accessibility
Ni–Co/Ni–Co–Ni	precursor layer architecture	1 M NaOH	Ni–Co–Ni: 111 mV dec^{-1}; −0.132 V at −10 mA cm^{-2}	layer order controls Co–Al/Ni–Al pathway and HER behaviour

Table 5. *Cont.*

System	Main Controlled Variable	Electrolyte	Representative Result	Main Conclusion
Ni–Pt/Ni–Pt–Ni	Pt exposure and distribution	10 wt% KOH	Ni–Pt: ca. 102 mV at −100 mA cm^{-2}; 32.2 mV dec^{-1}	exposed Pt-rich porous surface dominates HER/OER response
Porous coating on Ni temperature series, this work	molten-salt treatment temperature	1 M NaOH	825 °C gives highest provisional capacitance estimate; 900 °C gives lowest HER overpotentials	temperature gives different trends in capacitance estimates, HER response and OER behaviour

Note: Values were measured under different protocols and are used for contextual comparison only.

4. Conclusions

In this work, porous coatings were formed on compact Ni substrates by Co electrodeposition followed by Al deposition and anodic dissolution in molten salts at 750, 825 and 900 °C. The Co-coated Ni precursor, applied potentials and Al-deposition time were kept the same. The recorded anodic durations and transferred charges differed, so the comparison concerns the coatings obtained under these treatment conditions rather than temperature at matched charge and duration. At each temperature, the cathodic charge exceeded the anodic charge. This is consistent with incomplete Al removal but does not establish retained-Al content or phase identity.

Increasing treatment temperature changed the obtained coating from a fine and relatively thin porous layer at 750 °C to a thicker and coarser structure at 900 °C. The XRD patterns were dominated by fcc metallic reflections consistent with Co-rich material, with possible overlapping signals from Ni. Weak additional reflections were tentatively associated with Al-containing phases; the lower-angle feature in the 900 °C pattern remains unresolved. Local Al signals were registered by EDS, but signals in the resin outside the electrode were excluded from interpretation of the coating. The Al-containing phase was not identified.

The highest apparent capacitance estimate was obtained at 825 °C. Among the treated electrodes, the lowest HER and OER end-of-test overpotentials after 2 h were obtained at 900 °C, while the lowest apparent OER Tafel slope was obtained at 750 °C. The treatment temperature therefore gave different trends in capacitance and HER/OER response. The OER polarisation curves did not confirm a general improvement over unmodified Ni. These trends describe the individual measured electrodes and do not establish a statistically validated optimum temperature.

In our work, one selected electrode was compared for each treatment temperature. The sweep rate was 20 mV s^{-1}, no post-measurement iR correction was applied, and the chronopotentiometric measurements lasted 2 h. These measurements do not establish reproducibility between independently prepared electrodes or long-term durability. Easier electrolyte access and gas removal connected with the morphology remain possible explanations, rather than directly measured mechanisms. The statistical significance of differences in capacitance, apparent Tafel slopes and overpotentials was not established.

Author Contributions: D.K.: conceptualization, methodology, investigation, formal analysis, visualisation, writing—original draft, writing—review and editing. M.F.: conceptualization, methodology, resources, supervision, writing—review and editing. R.T.: investigation, data curation. K.S.: formal analysis, writing—review and editing. P.P.: investigation, data curation. P.Ż.: writing—review and editing. All authors have read and agreed to the published version of the manuscript.

Funding: This research was funded by the Yashima Environment Technology Foundation and financially supported by program "Excellence initiative—research university" for AGH University of

Krakow" (Grant no. 18004), IDUB AGH Activity 21. The funder had no role in the design of the study; in the collection, analysis and interpretation of data; in the writing of the manuscript; or in the decision to submit the article for publication.

Data Availability Statement: The raw and processed data supporting the findings of this study are available from the corresponding authors upon reasonable request.

Acknowledgments: During the preparation of this work, the authors used ChatGPT version 6.0 by OpenAI for language editing. After using this tool, the authors reviewed and edited the content as needed and take full responsibility for the content of the published article.

Conflicts of Interest: The authors declare that they have no known competing financial interests or personal relationships that could have appeared to influence the work reported in this paper.

References

1. Zeng, K.; Zhang, D. Recent progress in alkaline water electrolysis for hydrogen production and applications. *Prog. Energy Combust. Sci.* **2010**, *36*, 307–326. [CrossRef]
2. Ursúa, A.; Gandía, L.M.; Sanchis, P. Hydrogen production from water electrolysis: Current status and future trends. *Proc. IEEE* **2012**, *100*, 410–426. [CrossRef]
3. Carmo, M.; Fritz, D.L.; Mergel, J.; Stolten, D. A comprehensive review on PEM water electrolysis. *Int. J. Hydrogen Energy* **2013**, *38*, 4901–4934. [CrossRef]
4. Holladay, J.D.; Hu, J.; King, D.L.; Wang, Y. An overview of hydrogen production technologies. *Catal. Today* **2009**, *139*, 244–260. [CrossRef]
5. Hu, C.; Zhang, L.; Gong, J. Recent progress made in the mechanism comprehension and design of electrocatalysts for alkaline water splitting. *Energy Environ. Sci.* **2019**, *12*, 2620–2645. [CrossRef]
6. McCrory, C.C.L.; Jung, S.; Ferrer, I.M.; Chatman, S.M.; Peters, J.C.; Jaramillo, T.F. Benchmarking hydrogen evolving reaction and oxygen evolving reaction electrocatalysts for solar water splitting devices. *J. Am. Chem. Soc.* **2015**, *137*, 4347–4357. [CrossRef] [PubMed]
7. Shinagawa, T.; Garcia-Esparza, A.T.; Takanabe, K. Insight on Tafel slopes from a microkinetic analysis of aqueous electrocatalysis for energy conversion. *Sci. Rep.* **2015**, *5*, 13801. [CrossRef] [PubMed]
8. Subbaraman, R.; Tripkovic, D.; Strmcnik, D.; Chang, K.C.; Uchimura, M.; Paulikas, A.P.; Stamenkovic, V.; Markovic, N.M. Enhancing hydrogen evolution activity in water splitting by tailoring Li^+–$Ni(OH)_2$–Pt interfaces. *Science* **2011**, *334*, 1256–1260. [CrossRef] [PubMed]
9. Danilovic, N.; Subbaraman, R.; Strmcnik, D.; Chang, K.C.; Paulikas, A.P.; Stamenkovic, V.R.; Markovic, N.M. Enhancing the alkaline hydrogen evolution reaction activity through the bifunctionality of $Ni(OH)_2$/metal catalysts. *Angew. Chem. Int. Ed.* **2012**, *51*, 12495–12498. [CrossRef] [PubMed]
10. Sheng, W.; Myint, M.; Chen, J.G.; Yan, Y. Correlating the hydrogen evolution reaction activity in alkaline electrolytes with the hydrogen binding energy on monometallic surfaces. *Energy Environ. Sci.* **2013**, *6*, 1509–1512. [CrossRef]
11. Trasatti, S. Work function, electronegativity, and electrochemical behaviour of metals: III. Electrolytic hydrogen evolution in acid solutions. *J. Electroanal. Chem. Interfacial Electrochem.* **1972**, *39*, 163–184. [CrossRef]
12. Conway, B.E.; Tilak, B.V. Interfacial processes involving electrocatalytic evolution and oxidation of H_2 and O_2. *Electrochim. Acta* **2002**, *47*, 3571–3594. [CrossRef]
13. Corrigan, D.A. The catalysis of the oxygen evolution reaction by iron impurities in thin film nickel oxide electrodes. *J. Electrochem. Soc.* **1987**, *134*, 377–384. [CrossRef]
14. Trotochaud, L.; Young, S.L.; Ranney, J.K.; Boettcher, S.W. Nickel–iron oxyhydroxide oxygen-evolution electrocatalysts: The role of intentional and incidental iron incorporation. *J. Am. Chem. Soc.* **2014**, *136*, 6744–6753. [CrossRef] [PubMed]
15. Dionigi, F.; Strasser, P. NiFe-based (oxy)hydroxide catalysts for oxygen evolution reaction in non-acidic electrolytes. *Adv. Energy Mater.* **2016**, *6*, 1600621. [CrossRef]
16. Friebel, D.; Louie, M.W.; Bajdich, M.; Sanwald, K.E.; Cai, Y.; Wise, A.M.; Cheng, M.J.; Sokaras, D.; Weng, T.C.; Alonso-Mori, R.; et al. Identification of highly active Fe sites in (Ni,Fe)OOH for electrocatalytic water splitting. *J. Am. Chem. Soc.* **2015**, *137*, 1305–1313. [CrossRef] [PubMed]
17. Lupi, C.; Dell'Era, A.; Pasquali, M. Nickel–cobalt electrodeposited alloys for hydrogen evolution in alkaline media. *Int. J. Hydrogen Energy* **2009**, *34*, 2101–2106. [CrossRef]
18. Lupi, C.; Dell'Era, A.; Pasquali, M.; Imperatori, P. Composition, morphology, structural aspects and electrochemical properties of Ni–Co alloy coatings. *Surf. Coat. Technol.* **2011**, *205*, 5394–5399. [CrossRef]

19. González-Buch, C.; Herraiz-Cardona, I.; Ortega, E.; García-Antón, J.; Pérez-Herranz, V. Synthesis and characterization of macroporous Ni, Co and Ni–Co electrocatalytic deposits for hydrogen evolution reaction in alkaline media. *Int. J. Hydrogen Energy* **2013**, *38*, 10157–10169. [CrossRef]
20. Herraiz-Cardona, I.; Ortega, E.; Pérez-Herranz, V. Impedance study of hydrogen evolution on Ni/Zn and Ni–Co/Zn stainless steel based electrodeposits. *Electrochim. Acta* **2011**, *56*, 1308–1315. [CrossRef]
21. Herraiz-Cardona, I.; González-Buch, C.; Valero-Vidal, C.; Ortega, E.; Pérez-Herranz, V. Co-modification of Ni-based type Raney electrodeposits for hydrogen evolution reaction in alkaline media. *J. Power Sources* **2013**, *240*, 698–704. [CrossRef]
22. Navarro-Flores, E.; Chong, Z.; Omanovic, S. Characterization of Ni, NiMo, NiW and NiFe electroactive coatings as electrocatalysts for hydrogen evolution in an acidic medium. *J. Mol. Catal. A Chem.* **2005**, *226*, 179–197. [CrossRef]
23. Rami, A.; Lasia, A. Kinetics of hydrogen evolution on Ni–Al alloy electrodes. *J. Appl. Electrochem.* **1992**, *22*, 376–382. [CrossRef]
24. Birry, L.; Lasia, A. Studies of the hydrogen evolution reaction on Raney nickel–molybdenum electrodes. *J. Appl. Electrochem.* **2004**, *34*, 735–749. [CrossRef]
25. Brown, I.J.; Sotiropoulos, S. Preparation and characterization of microporous Ni coatings as hydrogen evolving cathodes. *J. Appl. Electrochem.* **2000**, *30*, 107–111. [CrossRef]
26. Chade, D.; Berlouis, L.; Infield, D.; Cruden, A.; Nielsen, P.T.; Mathiesen, T. Evaluation of Raney nickel electrodes prepared by atmospheric plasma spraying for alkaline water electrolysers. *Int. J. Hydrogen Energy* **2013**, *38*, 14380–14390. [CrossRef]
27. Bernäcker, C.I.; Rauscher, T.; Büttner, T.; Kieback, B.; Röntzsch, L. A powder metallurgy route to produce Raney-nickel electrodes for alkaline water electrolysis. *J. Electrochem. Soc.* **2019**, *166*, F357–F363. [CrossRef]
28. Dong, H.; Lei, T.; He, Y.; Xu, N.; Huang, B.; Liu, C.T. Electrochemical performance of porous Ni3Al electrodes for hydrogen evolution reaction. *Int. J. Hydrogen Energy* **2011**, *36*, 12112–12120. [CrossRef]
29. Tanaka, S.; Hirose, N.; Tanaki, T.; Ogata, Y.H. Effect of Ni–Al precursor alloy on the catalytic activity for a Raney-Ni cathode. *J. Electrochem. Soc.* **2000**, *147*, 2242–2245. [CrossRef]
30. Dulle, J.; Nemeth, S.; Skorb, E.V.; Irrgang, T.; Senker, J.; Kempe, R.; Fery, A.; Andreeva, D.V. Sonochemical activation of Al/Ni hydrogenation catalyst. *Adv. Funct. Mater.* **2012**, *22*, 3128–3135. [CrossRef]
31. Mullis, A.M.; Bigg, T.D.; Adkins, N.J. A microstructural investigation of gas atomized Raney type Al–27.5 at.% Ni catalyst precursor alloys. *J. Alloys Compd.* **2015**, *648*, 139–148. [CrossRef]
32. Erlebacher, J.; Aziz, M.J.; Karma, A.; Dimitrov, N.; Sieradzki, K. Evolution of nanoporosity in dealloying. *Nature* **2001**, *410*, 450–453. [CrossRef] [PubMed]
33. Qian, L.H.; Chen, M.W. Ultrafine nanoporous gold by low-temperature dealloying and kinetics of nanopore formation. *Appl. Phys. Lett.* **2007**, *91*, 083105. [CrossRef]
34. McCue, I.; Benn, E.; Gaskey, B.; Erlebacher, J. Dealloying and dealloyed materials. *Annu. Rev. Mater. Res.* **2016**, *46*, 263–286. [CrossRef]
35. Okamoto, H. Al–Ni (Aluminum–Nickel). *J. Phase Equilibria Diffus.* **2004**, *25*, 394. [CrossRef]
36. Ansara, I.; Dupin, N.; Lukas, H.L.; Sundman, B. Thermodynamic assessment of the Al–Ni system. *J. Alloys Compd.* **1997**, *247*, 20–30. [CrossRef]
37. Janssen, M.M.P.; Rieck, G.D. Reaction diffusion and Kirkendall-effect in the nickel–aluminum system. *Trans. Metall. Soc. AIME* **1967**, *239*, 1372–1385.
38. Adabi, M.; Amadeh, A.A. Formation mechanisms of Ni–Al intermetallics during heat treatment of Ni coating on 6061 Al substrate. *Trans. Nonferrous Met. Soc. China* **2015**, *25*, 3959–3966. [CrossRef]
39. Okamoto, H. Supplemental literature review of binary phase diagrams: Ag–Yb, Al–Co, Al–I, Co–Cr, Cs–Te, In–Sr, Mg–Tl, Mn–Pd, Mo–O, Mo–Re, Ni–Os, and V–Zr. *J. Phase Equilibria Diffus.* **2016**, *37*, 726–737. [CrossRef]
40. McAlister, A.J. The Al–Co (Aluminum–Cobalt) system. *Bull. Alloy Phase Diagr.* **1989**, *10*, 646–650. [CrossRef]
41. Nishizawa, T.; Ishida, K. The Co–Ni (Cobalt–Nickel) system. *Bull. Alloy Phase Diagr.* **1983**, *4*, 390–395. [CrossRef]
42. Raghavan, V. Al–Co–Ni (Aluminum–Cobalt–Nickel). *J. Phase Equilibria Diffus.* **2006**, *27*, 372–380. [CrossRef]
43. Šulhánek, P.; Drienovský, M.; Černičková, I.; Ďuriška, L.; Skaudžius, R.; Gerhátová, Ž.; Palcut, M. Oxidation of Al–Co alloys at high temperatures. *Materials* **2020**, *13*, 3152. [CrossRef] [PubMed]
44. Fukumoto, M.; Sugiuchi, K.; Nakajima, K. Formation of porous Ni surface by electrodeposition and dissolution in molten salt. *Int. J. Hydrogen Energy* **2020**, *45*, 28252–28259. [CrossRef]
45. Nakajima, K.; Fukumoto, M. Porous Ni–Co surface formation and analysis of hydrogen generation by gas sensor. *Int. J. Hydrogen Energy* **2021**, *46*, 26263–26271. [CrossRef]
46. Kutyła, D.; Nakajima, K.; Fukumoto, M.; Wojnicki, M.; Kołczyk-Siedlecka, K. Electrocatalytic performance of ethanol oxidation on Ni and Ni/Pd surface-decorated porous structures obtained by molten salts deposition/dissolution of Al–Ni alloys. *Int. J. Mol. Sci.* **2023**, *24*, 3836. [CrossRef] [PubMed]

47. Fukumoto, M.; Takahashi, H.; Kutyła, D.; Wojnicki, M.; Żabiński, P. Morphological investigation and electrochemical performance evaluation of novel porous Ni–Pt produced by Al-deposition/dissolution in molten salts for hydrogen and oxygen evolution reaction. *Int. J. Hydrogen Energy* **2024**, *49*, 754–765. [CrossRef]
48. Fukumoto, M.; Takahashi, H.; Kutyła, D.; Wojnicki, M.; Żabiński, P. Catalytic activity evaluation of molten salt-treated stainless steel electrodes for hydrogen evolution reaction in alkaline medium. *Coatings* **2024**, *14*, 796. [CrossRef]
49. Kutyła, D.; Fukumoto, M.; Takahashi, H.; Takahashi, R.; Skibińska, K.; Żabiński, P. Synthesis and evaluation of layered Ni–Co and Ni–Co–Ni electrodes modified by molten-salt Al deposition/dissolution technique for electrochemical applications. *Coatings* **2026**, *16*, 679. [CrossRef]
50. Skibińska, K.; Kutyła, D.; Marzec, M.M.; Wojtaszek, K.; Bardo, R.; Bała, P.; Żabiński, P. Effect of Al and Ti additions on the chronoamperometric oxidation of high-entropy alloys dedicated to electrooxidation of methanol. *Surf. Coat. Technol.* **2026**, *528*, 133441. [CrossRef]

Disclaimer/Publisher's Note: The statements, opinions and data contained in all publications are solely those of the individual author(s) and contributor(s) and not of MDPI and/or the editor(s). MDPI and/or the editor(s) disclaim responsibility for any injury to people or property resulting from any ideas, methods, instructions or products referred to in the content.